LANGMUIR

pubs.acs.org/Langmuir Article

CO_2 Adsorption Enhanced by Tuning the Layer Charge in a Clay Mineral

Kristoffer W. Bø Hunvik,* Patrick Loch, Dirk Wallacher, Alexsandro Kirch, Leide P. Cavalcanti, Martin Rieß, Matthias Daab, Vegard Josvanger, Sven Grätz, Fabiano Yokaichiya, Kenneth Dahl Knudsen, Caetano Rodrigues Miranda, Josef Breu, and Jon Otto Fossum*

Cite This: *Langmuir* 2021, 37, 14491−14499 Read Online

ACCESS | Metrics & More | Article Recommendations | Supporting Information

ABSTRACT: Due to the compact two-dimensional interlayer pore space and the high density of interlayer molecular adsorption sites, clay minerals are competitive adsorption materials for carbon dioxide capture. We demonstrate that with a decreasing interlayer surface charge in a clay mineral, the adsorption capacity for CO_2 increases, while the pressure threshold for adsorption and swelling in response to CO_2 decreases. Synthetic nickel-exchanged fluorohectorite was investigated with three different layer charges varying from 0.3 to 0.7 per formula unit of $Si_4O_{10}F_2$. We associate the mechanism for the higher CO_2 adsorption with more accessible space and adsorption sites for CO_2 within the interlayers. The low onset pressure for the lower-charge clay is attributed to weaker cohesion due to the attractive electrostatic forces between the layers. The excess adsorption capacity of the clay is measured to be 8.6, 6.5, and 4.5 wt % for the lowest, intermediate, and highest layer charges, respectively. Upon release of CO_2, the highest-layer charge clay retains significantly more CO_2. This pressure hysteresis is related to the same cohesion mechanism, where CO_2 is first released from the edges of the particles thereby closing exit paths and trapping the molecules in the center of the clay particles.

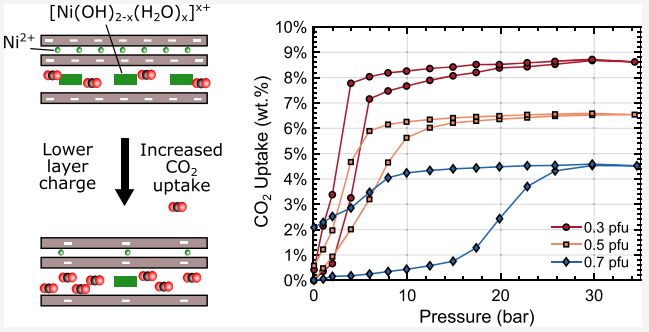

INTRODUCTION

To mitigate greenhouse gas emissions, new technologies are required. As they are cheap, abundant, good CO_2 adsorbers,[1−15] and present in cap-rock formations for carbon storage sites,[16] smectite clay minerals are particularly important in this context. Understanding how carbon dioxide can selectively adsorb in the interlayers of clay minerals and tuning those mechanisms could both pave the way for new adsorbent materials and improve our understanding of the long-term stability of anthropogenic storage sites.

Smectite clay minerals are phyllosilicates consisting of 2:1 nanolayers built from two tetrahedral sheets sandwiching an octahedral sheet. Isomorphic substitutions in the tetrahedral or octahedral sheet cause a permanent charge of the 2:1 layer that is compensated by cations in the interlayer space. In dried smectite clay minerals, the two-dimensional interlayers are separated by ∼1 nm, providing ∼1000 km^2 of accessible surface area per cubic meter of clay material. Within the interlayers there is a high density of molecular adsorption sites.[17] The mechanism for molecular adsorption depends on the interlayer species at each adsorption site and their affinity for specific molecules. This means that the volumetric capacity for molecular adsorption in smectite clay minerals can be very high. In particular, this renders smectite clay minerals very competitive for CO_2 capture, which was recently shown experimentally.[15]

Depending on their layer charge, these silicates can be divided into smectites, with a layer charge of 0.2−0.6 per formula unit (pfu) of $Si_40_{10}F_2$, and vermiculites, with a layer charge in the range of 0.6−0.9 pfu.[17] The influence of the layer charge on the hydration properties of clay minerals has attracted considerable interest.[18−25] Simulations on montmorillonite suggested that a higher layer charge facilitates the entry of water molecules into the clay interlayers and decreases CO_2 adsorption, while a higher $CO_2/(CO_2 + H_2O)$ mole fraction is acquired when the charge is low.[26] However, a systematic experimental study of how the layer charge influences CO_2 adsorption in clay minerals has thus far not been conducted. Layer charge has been shown to have an effect on the adsorption of CH_4 in hectorite,[27] where a lower layer charge enhances CH_4 adsorption.

Received: September 20, 2021
Revised: November 15, 2021
Published: December 1, 2021

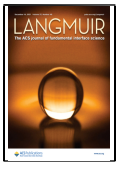

https://doi.org/10.1021/acs.langmuir.1c02467
Langmuir 2021, 37, 14491−14499

In this work, we investigate the role of the layer charge in CO_2 uptake and swelling in a synthetic clay mineral, fluorohectorite intercalated with nickel (Ni-Hec). Synthetic Hec shows a homogeneous charge density and, consequently, a uniform intracrystalline reactivity.[28] It can be synthesized as large defect free particles,[29] providing an excellent template for studying interactions with CO_2 without the interference of defects or impurities. Ni-Hec has recently been shown to form a corrensite-like structure, with an ordered interstratifaction of chlorite-like layers with a composition of $[Ni(OH)_{0.83}(H_2O)_{1.17}]_{0.37}^{1.17+}$, and hydrated smectite-like layers with Ni^{2+} cations.[30] For this clay mineral, the hydration follows an atypical, partly continuous swelling behavior, which is related to the chlorite-like phase in the interlayer.[30,31] The chlorite-like phase has also been demonstrated to be responsible for CO_2 adsorption, where the molecules form a reversible bond with the intercalated nickel hydroxide.[14] The CO_2 could be grafted as a bicarbonate to the condensed nickel hydroxide species.[14] To investigate the layer charge dependency in a systematic manner, we have conducted X-ray and neutron diffraction and gravimetric adsorption measurements on dry Ni-Hec prepared with three different layer charges, 0.3, 0.5, and 0.7 pfu. The samples were dried to at least 120 °C to ensure the removal of interlayer water and water coordinated to uncondensed interlayer cations, while preserving the clay layers and the nickel hydroxide in the chlorite-like layers.[30] The experimental measurements are supported by first-principles calculations performed within the density functional theory (DFT) approach.

MATERIALS AND METHODS

Materials. Na-fluorohectorite (Na-Hec) with a nominal composition of $Na_x(Mg_{3-x}Li_x)Si_4O_{10}F_2$ (x = 0.5 and 0.7) was prepared via melt synthesis according to published procedures.[29,32] Therefore, the synthesis was carried out in gastight molybdenum crucibles. NaF (99.995%, Alfa Aesar), LiF (>99.9%, ChemPur), MgF_2 (>99.9%, ChemPur), MgO (99.95%, Alfa Aesar), and SiO_2 (Merck, fine granular quartz, purum) were mixed according to the nominal composition of Na-Hec. The crucible was heated to 1750 °C (15 °C/min), held at this temperature for 70 min, cooled to 1300 °C (55 °C/min) and then to 1050 °C (10 °C/min), and finally quenched by switching of the power. Subsequent long-term annealing was used to improve charge homogeneity and phase purity, resulting in phase pure and layer charge homogeneous materials. Na-fluorohectorite with x = 0.3 ($Na\text{-}Hec_{0.3}$) was prepared after layer charge reduction of $Na\text{-}Hec_{0.5}$ after repeated Mg exchange employing the Hofmann−Klemen effect.[33] The layer charge was checked according to the literature.[34] The cation exchange capacity (CEC) was determined using $BaCl_2$ following DIN ISO 11260 and determined to be 75, 129, and 185 mequiv/100 g for layer charges of 0.3, 0.5, and 0.7 pfu, respectively. These results are in agreement with calculated values of 78, 130, and 194 mequiv/100 g, respectively. Ni-Hec was prepared by cation exchange of Na-Hec with a 0.2 M nickel acetate solution (>10-fold excess of the CEC, five times), following a published procedure.[30] The exchanged Ni-Hec was washed five times with Millipore water.

Cation exchange of Ni-Hec with a long-chain n-alkylammonium solution (C16, $C_{16}H_{33}NH_3Cl$) was performed with a 10-fold excess of CEC (80 °C, three times) to ensure complete exchange. The obtained C16-exchanged Ni-Hec was washed five times with ethanol/water (1:1) and once with ethanol (p.a.) and then dried at 80 °C. The composition of $Ni\text{-}Hec_x$ (x = 0.3 and 0.7) was determined via inductively coupled plasma atomic emission spectroscopy (ICP-OES) according to Loch et al.,[30] comparing the Ni content of the pristine and C16-exchanged $Ni\text{-}Hec_x$. Approximately 20 mg of $Ni\text{-}Hec_x$ equilibrated at a relative humidity of 43% was weighed into 15 mL clean Teflon flasks. C16-exchanged $Ni\text{-}Hec_x$ was dried at 80 °C prior to the measurement. After addition of 1.5 mL of 30 wt % HCl (Merck), 0.5 mL of 85 wt % H_3PO_4 (Merck), 0.5 mL of 65 wt % HNO_3 (Merck), and 1 mL of 48 wt % HBF_4 (Merck), the sample was digested in a MLS 1200 Mega microwave digestion apparatus for 6.5 min and heated at 600 W (MLS GmbH, Mikrowellen-Labor-Systeme, Leutkirch, Germany). The closed sample container was cooled to room temperature, and the clear solution was diluted to 100 mL in a volumetric flask and analyzed on a PerkinElmer Avio 200 spectrometer.

Powder X-ray Diffraction. Powder X-ray diffraction (PXRD) experiments during adsorption of CO_2 were conducted at the KMC-2 beamline of the BESSY II light source at Helmholtz-Zentrum Berlin.[35] A capillary-based sample cell system, centered in the synchrotron beam, was connected to a gas dosing system (Teledyne ISCO 260D). The temperature of the sample was directly measured by a K-type thermocouple mounted close to the measurement point and connected to a Eurotherm indicator unit 32h8i. A 0.01 mm wall thickness quartz capillary (Hilgenberg) with a diameter of 0.5 mm was glued in a $^1/_4$ in. VCR weld gland (Swagelok). Before the measurements, the samples were filled in capillaries and dried for at least 2 h at 150 °C under high vacuum (10^{-6} mbar) in an *ex situ* dedicated capillary drying station. Subsequently, it was connected via a Swagelok thread to the gas handling system providing CO_2 of quality N55 (99.9995%). All *in situ* measurements were carried out at 26 °C. The diffraction experiments were conducted in transmission geometry in the 2θ range of 2.5−14.5° using monochromatic synchrotron radiation (λ = 1.5406 Å). A full 360° rotation of the capillary in the beam was implemented by a script-controlled step motor. The diffraction images from the two-dimensional detector (Bruker Våntec 2000) were integrated using proprietary software. NIST silicon SRM 640a was used as the external standard for peak positions.

Gravimetric Adsorption. CO_2 adsorption measurements were conducted with an IsoSORP gravimetric sorption analyzer from Rubotherm. Each sample was prepared by being degassed at 120 ± 5 °C overnight under high vacuum. For each sample, three measurements were conducted with equilibration times of 1, 2, or 4 h at each pressure step from vacuum to 35 bar. The temperature was measured with a Pt-100 sensor placed directly underneath the sample crucible. It was surrounded by a double-walled thermostat controlled by a circulating water bath CC-K6 from Huber. The temperature stability of the sample was within 22.5 ± 1 °C. The suspension balance has a resolution of 0.01 mg and a reproducibility of <0.002% rdg (≈0.002 mg). The data for pressure, temperature, and sample weight were continuously recorded. The measured quantity is the excess adsorbed amount, which is obtained by correcting for the buoyancy of the skeletal volume of the sample material and the suspended metal parts (including the sample holder). The skeletal volume of the three samples was determined by individual helium isotherms. The buoyancy of the suspended metal parts was obtained by a blank measurement with CO_2. The densities of helium and CO_2 for the given pressure and temperature conditions were obtained from the equation of state data provided by NIST.[36]

Computational Methodology. First-principles calculations based on the DFT were conducted to evaluate basal separation distances and adsorption energies. The simulations were performed using the Siesta package.[37] The double-zeta plus polarization (DZP) and spin-polarized localized atomic orbital basis sets with a 400 Ry energy cutoff were used. The corrected generalized gradient approximation developed by Berland and Hyldgaard[38] was employed to account for the van der Waals interactions. On the basis of the crystallographic structure of our previous work,[14] the layer charges were modified by substituting Mg with Li atoms in the supercell (multiple unit cells). We systematically explored four layer charges (0.25, 0.5, 0.75, and 1.0 pfu), which were chosen to resemble the experimental stoichiometry. These charges were balanced with the interlayer Ni cations. For each stoichiometry, distinct Li and Ni interlayer atomic sites were fully considered and sampled for total energy minimization.

https://doi.org/10.1021/acs.langmuir.1c02467
Langmuir 2021, 37, 14491−14499

RESULTS AND DISCUSSION

Structure Determination. Ni-Hec$_{0.5}$ forms an ordered interstratification of a condensed $[Ni(OH)_{0.83}(H_2O)_{1.17}]_{0.37}^{1.17+}$ species in one interlayer and hydrated Ni^{2+} cations in the adjacent layer.[30] Due to the similar electron densities of the two interlayer species, the superstructure reflection is expected to be weak and was therefore amplified by enhancing the electron contrast of the interlayers. Cation exchange of the noncondensed Ni^{2+} interlayer cations with long-chain *n*-alkylammonium (C16, $C_{16}H_{33}NH_3Cl$) led to a clearly visible superstructure as observed by PXRD.[30] This procedure was used to identify a comparable condensed species and a possible superstructure in Ni-Hec$_{0.7}$ and Ni-Hec$_{0.3}$.

Similar to Ni-Hec$_{0.5}$ (Figure 7 of ref 30), C16-exchanged Ni-Hec$_{0.7}$ shows a clearly visible reflection of an ordered interstratified superstructure (Figure S1). The basal spacing of 40.5 Å [coefficient of variation (CV) of 0.79] can be explained by the formation of an ordered interstratification of two strictly alternating interlayer species. The condensed nickel hydroxide species with a basal spacing of 14.5 Å and a paraffin-like arrangement of C16 cations with a basal spacing of 26 Å form a corrensite-like structure during the C16-exchange. The chemical composition was determined with ICP-OES according to Loch et al.,[30] giving a composition of $[[Ni(OH)_{1.49}(H_2O)_{0.58}]_{0.53}^{0.58+}]_{Int.1}$ $[[Ni(H_2O)_6]_{0.38}^{2+}]_{Int.2}$ $[Mg_{4.6}Li_{1.4}]\langle Si_8\rangle O_{20}F_4$ for Ni-Hec$_{0.7}$.

Na-Hec$_{0.3}$, which was used for the preparation of Ni-Hec$_{0.3}$, cannot be obtained directly from melt synthesis. Thus, it requires a layer charge reduction procedure prior to cation exchange,[39] which in turn lowers the layer charge homogeneity compared to those of Ni-Hec$_{0.5}$ and Ni-Hec$_{0.7}$. Therefore, C16-exchanged Ni-Hec$_{0.3}$ showed no superstructure reflection (Figure S2). A basal spacing of 17.7 Å (CV = 0.42) is characteristic for a bilayer arrangement of C16[33,34,40] in the interlayer space, indicating an occupation of C16 in every interlayer, and is in accordance with the layer charge of 0.3 pfu. The structure can consequently be seen as a random interstratification of condensed and noncondensed interlayer species with a composition of $[[Ni(OH)_{1.10}(H_2O)_{0.90}]_{0.10}^{0.90+}]_{Int.1}$ $[[Ni(H_2O)_6]_{0.25}^{2+}]_{Int.2}$ $[Mg_{5.4}Li_{0.6}]\langle Si_8\rangle O_{20}F_4$.

***In Situ* Powder X-ray Diffraction.** The evolution of the (001) or (002) Bragg reflection upon CO_2 exposure for Ni-Hec$_x$ dried at 150 °C with a layer charge of 0.3, 0.5, and 0.7 pfu is shown in Figures 1−3. As no ordered superstructure is observed for Ni-Hec$_{0.3}$ after C16 exchange, these results represent the (001) Bragg reflection of a random interstratification (Figure 1), while for Ni-Hec$_{0.5}$ and Ni-Hec$_{0.7}$, it corresponds to the (002) reflection of an ordered interstratification (Figures 2 and 3). Similar to what was observed for Ni-Hec$_{0.5}$ by Hunvik et al.,[14] with an increasing pressure of CO_2 the Bragg reflection moves to lower q values as a result of the swelling process. Swelling is an inherent one-dimensional process, in which the Bragg reflections gradually move as the number of swollen interlayers increases and thus the relative contribution of the interstratified stacks becomes larger.

For dried Ni-Hec$_{0.3}$, initially an asymmetric (001) Bragg reflection at 0.563 $Å^{-1}$ (d_{001} = 11.15 Å) under vacuum (0.07 bar) is observed (Figure 1). During the CO_2 exposure, no changes were observed at 1 and 2 bar of CO_2. As the pressure is increased to 5 bar, the peak gradually shifts, and the sample

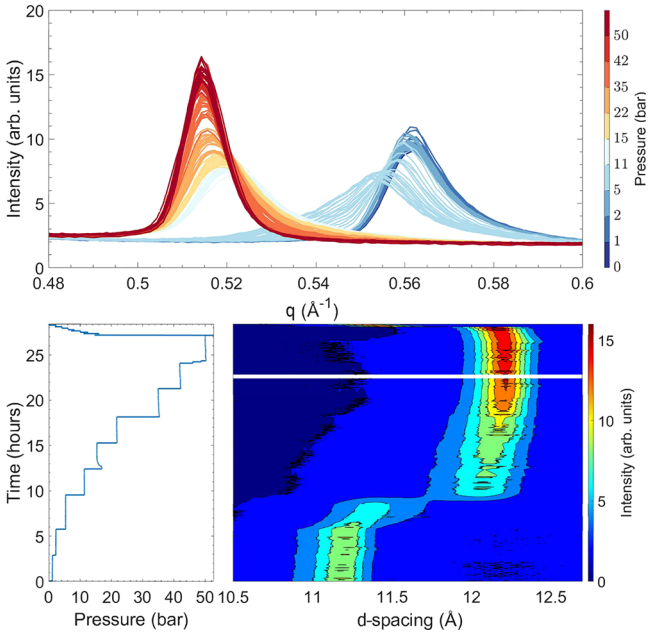

Figure 1. Evolution of the (001) Bragg reflection as a function of pressure at 26 °C for Ni-Hec$_{0.3}$ recorded via PXRD. The bottom left panel shows the measured pressure of CO_2 applied on the sample as a function of time, and the bottom right panel shows a contour plot in which the horizontal axis corresponds to the d spacing ($d = 2\pi/q$). The vertical axis corresponds to time scaled by the same horizontal axis as for the pressure, and the color gradient represents the intensity. In the top panel, the evolution of the (001) Bragg reflection is plotted with colors indicating the approximate pressure.

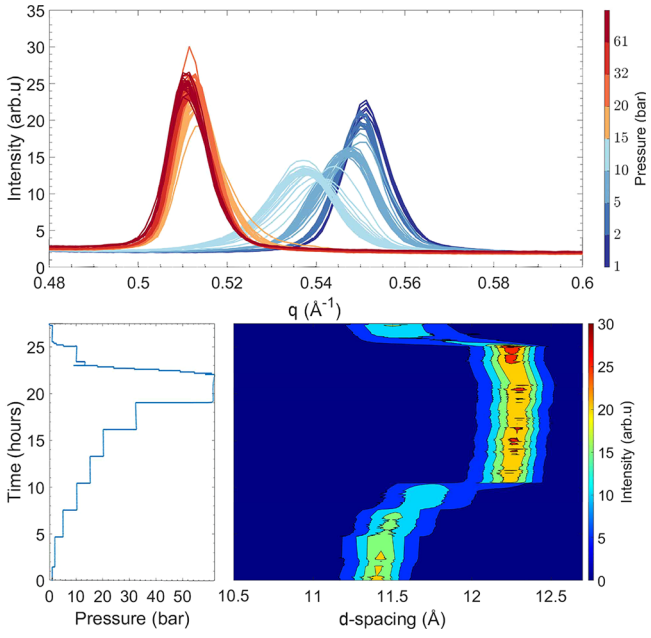

Figure 2. Evolution of the (002) Bragg reflection as a function of pressure at 26 °C for Ni-Hec$_{0.5}$ recorded via PXRD. The bottom left panel shows the measured pressure of CO_2 applied on the sample as a function of time, and the bottom right panel shows a contour plot in which the horizontal axis corresponds to d spacing ($d = 2\pi/q$). The vertical axis corresponds to time scaled by the same horizontal axis as for the pressure, and the color gradient represents the intensity. In the top panel, the evolution of the (002) Bragg reflection is plotted with colors indicating the approximate pressure.

https://doi.org/10.1021/acs.langmuir.1c02467
Langmuir 2021, 37, 14491−14499

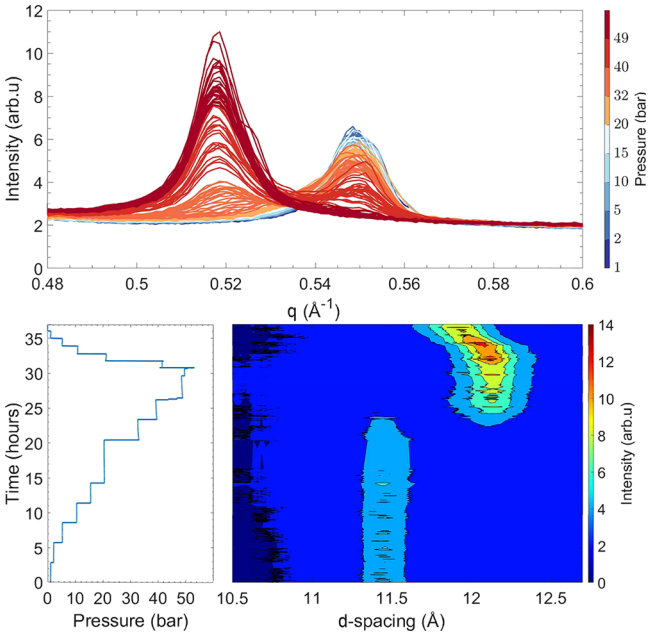

Figure 3. Evolution of the (002) Bragg reflection as a function of pressure at 26 °C for Ni-Hec$_{0.7}$ recorded via PXRD. The bottom left panel shows the measured pressure of CO_2 applied on the sample as a function of time, and the bottom right panel shows a contour plot in which the horizontal axis corresponds to the d spacing ($d = 2\pi/q$). The vertical axis corresponds to time scaled by the same horizontal axis as for the pressure, and the color gradient represents the intensity. In the top panel, the evolution of (002) Bragg reflection is plotted with colors indicating the approximate pressure.

starts to swell. At 11 bar, the intensity is shifted from the educt to the product phase, slowly becoming more symmetric toward the final pressure. At the final pressure of 50 bar of CO_2, a symmetric (001) Bragg reflection at 0.514 Å^{-1} (d_{001} = 12.21 Å) is observed. The pressure was released quickly after CO_2 exposure, and a symmetric peak appears, centered at 0.556 Å^{-1} (d_{001} = 11.30 Å) (Figure S3). The symmetric peak indicates a higher-order stacked structure, while the value of the basal spacing reveals the release of most of the CO_2.

For dried Ni-Hec$_{0.5}$, initially a symmetric peak at 0.551 Å^{-1} (d_{002} = 11.39 Å) is observed, corresponding to the (002) reflection of the ordered interstratified structure (Figure 2). Similar to the observation of Hunvik et al.,[14] up to 10 bar the shifts are marginal for each pressure step. At 10 bar, the reflection gradually shifts toward the product phase, ending up at 15 bar as a symmetric peak with only minor changes, before reaching the final pressure. At the final pressure of 60 bar, a symmetric peak at 0.512 Å^{-1} (d_{002} = 12.26 Å) is observed. When the the pressure is decreased, CO_2 is released and the reflection shifts back to 0.547 Å^{-1} (d_{002} = 11.48 Å), forming a significantly broader peak at higher d spacings compared to that of the initial state. Compared to Ni-Hec$_{0.3}$, the onset of swelling is located at a higher pressure, while the end state after pressure is decreased is less ordered, as judged from the peak broadening. This is likely a result of some interlayers still retaining CO_2 (discussed below) and suggests that the cohesion of the layers in this case is stronger than that in Ni-Hec$_{0.3}$, preventing the complete desorption of CO_2. Included in the Supporting Information are neutron diffraction measurements (Figures S4 and S5), where the sample was given more time to equilibrate. Consequently, it is clear that Ni-Hec$_{0.5}$ returns to its initial state given enough time under vacuum (0.003 bar), which confirms the influence of the higher layer charge on CO_2 adsorption.

For dried Ni-Hec$_{0.7}$, a symmetric (002) Bragg reflection of the corrensite structure at 0.548 Å^{-1} (d_{002} = 11.45 Å) is observed (Figure 3). During the exposure to CO_2, the peak shape remains almost unchanged until the pressure reaches 32 bar, when the level of the product phase starts to increase at the expense of the educt phase. At the final pressure of 50 bar, a symmetric peak at 0.518 Å^{-1} (d_{002} = 12.11 Å) is observed. When the pressure is subsequently reduced, the (002) Bragg reflection slowly returns to higher q values, corresponding to a decrease in the basal spacing. However, the sample does not reach its initial state and a broad peak centered at 0.527 Å^{-1} (d_{002} = 11.90 Å) is observed, which is even broader than in Ni-Hec$_{0.5}$. Again, swelling and shrinking in response to CO_2 result in two well-defined states, where the onset is at an even higher pressure than for the two previous samples with lower layer charges (0.3 and 0.5 pfu).

For the X-ray diffraction experiments, the equilibration time was shorter than for the neutron diffraction experiments (Figure S6). In the latter case, when the pressure is decreased, the basal spacing of Ni-Hec$_{0.7}$ does not return to its initial state, indicating a certain retention of CO_2 even after longer equilibration times at low pressure. Consequently, the higher layer charge also assists in the retention of CO_2 and confirms the influence of the layer charge on the swelling process.

The three samples are compared in Figure 4, where the d spacing of the most intense peak of the (001)/(002) Bragg reflection as a function of pressure is shown. It is evident from the discussion above and Figure 4 that Ni-Hec with a higher layer charge shows a higher onset pressure for swelling upon CO_2 exposure and, concomitantly, greater retention of the CO_2. This results in a larger hysteresis loop starting from Ni-Hec$_{0.3}$ to Ni-Hec$_{0.7}$, where Ni-Hec$_{0.7}$ clearly resides in a partly swollen state even after the CO_2 pressure is decreased. The slightly higher basal spacings of Ni-Hec$_{0.3}$ and Ni-Hec$_{0.5}$ might indicate a certain retention of CO_2 but are negligible compared to that of Ni-Hec$_{0.7}$ and can be due to a higher stacking order or differences in the degree of condensation of the chlorite-like layers.

Gravimetric Adsorption. To quantify CO_2 uptake as a function of the layer charge of Ni-Hec, gravimetric adsorption measurements were performed. The gravimetric excess sorption of Ni-Hec with the three different layer charges is shown in Figure 5. The respective densities obtained from an He isotherm are listed in Table S1. In agreement with the PXRD results, the adsorption should largely take place in the interlayer space, as the N_2 physisorption isotherm for Ni-Hec$_{0.5}$ (Figure S7) shows only limited adsorption and no significant BET surface area (1.8 m^2/g). Included in Figure S8 are gravimetric data where the equilibration time at each pressure step is 1, 2, and 4 h. We observed that the equilibration time has no effect on Ni-Hec$_{0.3}$. For Ni-Hec$_{0.5}$ and Ni-Hec$_{0.7}$, a dependency on equilibration is noticed in the decrease in the size of the hysteresis loop with an increase in the equilibration time. However, for all samples, the final uptake is unaffected by exposure to CO_2 with these equilibration times. The additional buoyancy due to the increase in volume by the clay swelling in response to CO_2 is not included in the data presented in Figure 5. At the final pressure with a fully swollen state, this will add an additional 3−4% to the final excess adsorption capacity.

https://doi.org/10.1021/acs.langmuir.1c02467
Langmuir 2021, 37, 14491−14499

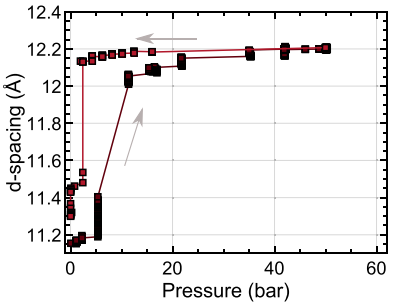

(a) Ni-Hec$_{0.3}$

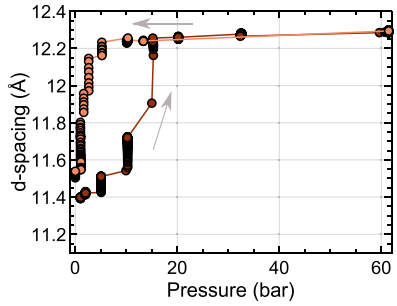

(b) Ni-Hec$_{0.5}$

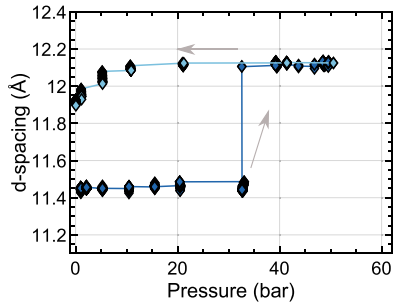

(c) Ni-Hec$_{0.7}$

Figure 4. Evolution of the most prominent feature of the (001)/(002) Bragg reflection as a function of pressure at 26 °C for Ni-Hec$_{0.3}$, Ni-Hec$_{0.5}$, and Ni-Hec$_{0.7}$. The arrows show the swelling hysteresis with the increase or decrease in pressure.

For Ni-Hec$_{0.3}$ (Figure 5), the uptake of CO_2 starts immediately between 2 and 6 bar. The uptake rises only slightly above 6 bar, until the curve flattens around 20 bar, achieving a maximum uptake of 8.6 wt % (2.14 mmol/g) at 35 bar. Upon desorption, no significant mass loss was observed until approximately 4 bar. Below that point, a large step occurred and most of the CO_2 is released when the lowest pressure (0.02 bar) is reached. For Ni-Hec$_{0.5}$ (Figure 5), the uptake starts immediately similar to Ni-Hec$_{0.3}$ and follows a continuous trend up to ~12 bar, where the curve starts to flatten out. At 35 bar, a maximum excess adsorption of 6.5 wt % (1.59 mmol/g) was achieved, lower than the uptake observed for Ni-Hec$_{0.3}$. Upon desorption, only a small mass loss until approximately 8 bar can be observed, after which most of the CO_2 is released at the lowest pressure (0.01 bar) and approximately 0.5 wt % CO_2 remained in the sample. For Ni-Hec$_{0.7}$ (Figure 5), only a minor uptake before 13 bar is found, which significantly increases until 30 bar after which the curve flattens. At 35 bar, a maximum excess adsorption of 4.5 wt %, 1.08 mmol/g, is observed. Upon desorption, the sample does not release any significant amount of CO_2 above 12 bar.

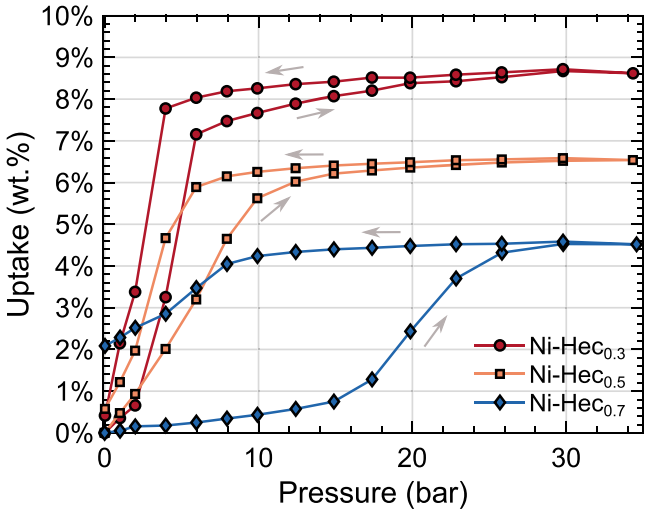

Figure 5. Comparison of the gravimetric adsorption capacity in dried Ni-Hec with layer charges Ni-Hec$_{0.3}$, Ni-Hec$_{0.5}$, and Ni-Hec$_{0.7}$ equilibrated for 4 h at each pressure step. The arrows show the sorption hysteresis with the increase or decrease in pressure.

Ultimately, between 2 and 2.5 wt % of CO_2 was retained in the sample.

The shape of the adsorption isotherms resembles that of the water adsorption isotherms for Na-Hec,[28,41] where the adsorption occurs between two discrete states. Due to the limited adsorption of Ni-Hec$_{0.7}$ before the pressure threshold, any significant adsorption of CO_2 in the bulk can be ruled out, which would otherwise produce a more gradual adsorption isotherm. This is consistent with the swelling observed by *in situ* PXRD that occurs only between two defined states.

In terms of uptake, layer charge plays a distinct role, with a higher uptake for a lower layer charge. At 35 bar, the CO_2 uptake values are 8.6, 6.5, and 4.5 wt % for Ni-Hec with layer charges of 0.3, 0.5, and 0.7 pfu, respectively. Previously, we demonstrated that the adsorption mechanism in Ni-Hec$_{0.5}$ is controlled by an interaction with the $[Ni(OH)_{0.83}(H_2O)_{1.17}]_{0.37}^{1.17+}$ species in the interlayer,[14] and the Ni^{2+} cations in the smectite-like layers are unresponsive to CO_2 under anhydrous conditions. For the low-charge clay, less interlayer species is required to counterbalance the layer charge, and therefore, more space is available in the interlayer for CO_2. This is also confirmed by the measured lower density from the He isotherm (Table S1) for the lower-charge clay, because greater formation of nickel hydroxide would result in a higher density. Given the low density of $[[Ni(OH)_{1.10}(H_2O)_{0.90}]_{0.10}^{0.90+}]$ species for Ni-Hec$_{0.3}$ some of the CO_2 may be attached to the interlayer species, and some may be occupying the interlayer space available between the condensed islands. Previous observations of CH_4 adsorption in hectorite with varying layer charges find greater CH_4 adsorption for a lower layer charge.[7] In accordance with our conclusions, this was related to more pore space being available due to fewer cations being required in the interlayer to balance the lower layer charge.

The hysteresis behavior is also influenced by the layer charge. Ni-Hec$_{0.7}$ (Figure 5) starts adsorbing at much higher pressures than the two other samples. A difference is also apparent in that for the lower-charge samples (Ni-Hec$_{0.3}$ and Ni-Hec$_{0.5}$) almost all of the CO_2 can be released, whereas in the case of the high layer charge (Ni-Hec$_{0.7}$), CO_2 remains in

https://doi.org/10.1021/acs.langmuir.1c02467
Langmuir 2021, 37, 14491−14499

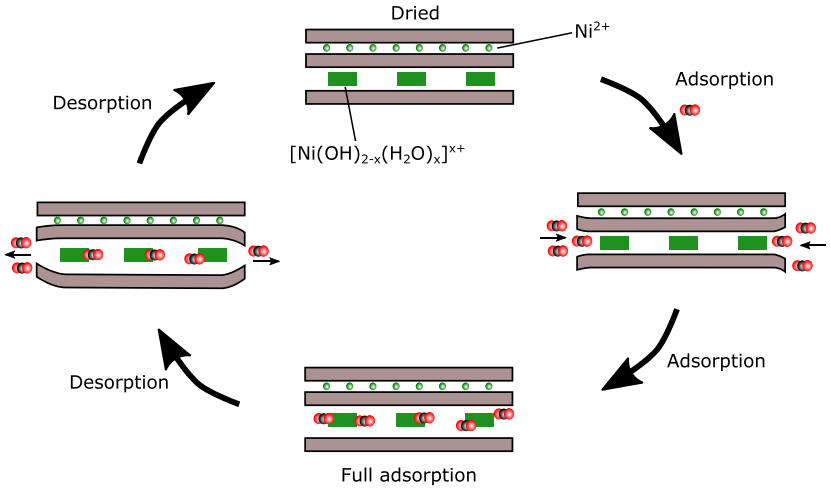

Figure 6. Sketch of the CO_2 adsorption process in clay. The CO_2 penetrates the clay from the edges of the clay platelet, slowly expanding the clay as the CO_2 enters. At full adsorption, the clay is fully expanded. As the pressure is decreased, the CO_2 molecules close to the edges are the first to leave the clay, forming a pocket inside with trapped CO_2. With a decrease in the pressure and given enough time, the clay will slowly return to its initial dry and collapsed state.

the sample under the used conditions. A higher layer charge results in stronger electrostatic cohesion between the clay layers, creating a higher energy barrier for the CO_2 to enter the interlayer. A possible mechanism is illustrated in Figure 6, showing swelling that first occurs from the edges of the clay particle. Upon desorption, the CO_2 first leaves from regions near the edges. This could partially close the exit paths, trapping some of the CO_2 by the electrostatic cohesion of the layers. This effect would be more important for a higher layer charge and, consequently, result in the greater retention we observe. This is similar to the so-called "ring mechanism" proposed by Weiss et al.[42] for kaolinite intercalation, which was also observed for Hec by Stöcker et al.[43] Due to the large size of the tactoid, intercalation occurs along all edges of the particle instead of via a "one-sided wedge" mechanism.

These results show a larger dependency on layer charge for CO_2 adsorption and swelling compared to what has been observed for H_2O adsorption and/or swelling.[18,19] The crystalline swelling upon hydration of clays depends on the Coulombic and van der Waals attraction, hydration and Born repulsion and is inherently hysteretic.[44] For synthetic saponites, where the charge is located in the tetrahedral sheet, swelling upon exposure to water occurs at lower values of relative humidity as the layer charge increases.[18] In addition, the increase in layer charge led to an increasing amount of water adsorbed in this clay mineral, due to the larger amount of interlayer cations allowing greater hydration.[18] For hectorite, on the contrary, with an origin of the layer charge in the octahedral sheet, the water adsorption isotherms and the amount of water adsorbed were independent of the location and the amount of layer charge.[19] Water strongly interacts with the interlayer cation, an interaction that is significantly stronger than the Coulomb attraction between the layers and the interlayer cation. For CO_2, there is a weaker interaction with the interlayer species than for water. The resulting layer−layer repulsion force from the presence of CO_2 could then be comparable to the Coulomb attraction, which could explain the large dependency of layer charge for CO_2 swelling as opposed to the H_2O case.

DFT Calculations. This interpretation is reinforced by DFT simulations of the system. The cohesion energy of the layers significantly increases with layer charge (Figure 7). For the chlorite-like layer where the CO_2 is believed to enter, the

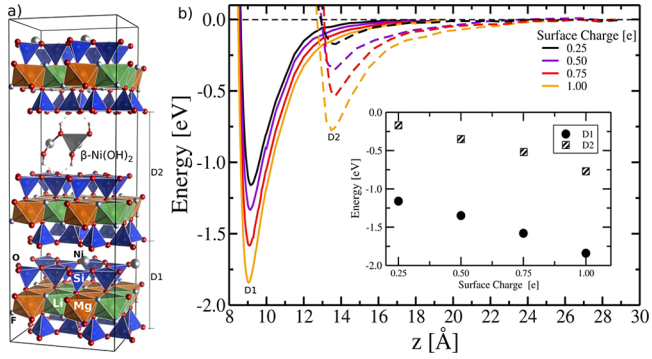

Figure 7. (a) Side view of the Hec molecular model highlighting the atomic configuration with a layer charge of 1.0 pfu (unit cell area of 9.2 Å × 5.3 Å) achieved by the substitution of two Mg atoms with Li atoms. (b) Energy curves for the dehydrated smectite (D_1) and for the β-Ni(OH)$_2$ island (D_2) in the interlayer space considering the role of the surface charges. The equilibrium position indicates the basal separation distance, while the depth of the potential well may be interpreted as the cohesion energy per unit cell. The basal d spacing can be obtained by the term $(D_1 + D_2)/2$. The inset shows the energy minimum as a function of surface charge.

value of the energy minimum more than doubles. In addition, basal separation distances were determined as a function of the surface charge. We observed that the equilibrium configurations of dried smectites have a minor dependence (<0.1 Å) on the surface charge, which is in agreement with previous studies.[26]

Comparison to Other Systems. To compare our results with similar measurements on a commercial Ni-exchanged Hec from Corning by Cavalcanti et al.,[15] where the bulk density (≈0.7 g/cm^3) of the samples was used to estimate the effective volume, we have to use the density acquired from an He isotherm. The final uptake in Cavalcanti et al.[15] is readjusted to 7 wt %, by assuming that the density is the same as that of our current Ni-Hec$_{0.7}$. The uptake behavior for this sample is in accordance with our observed layer charge dependence, as

https://doi.org/10.1021/acs.langmuir.1c02467
Langmuir 2021, 37, 14491−14499

shown in Figure 8, because the sample of Cavalcanti et al.[15] has a layer charge of ∼0.6 pfu on average. Still, a direct comparison

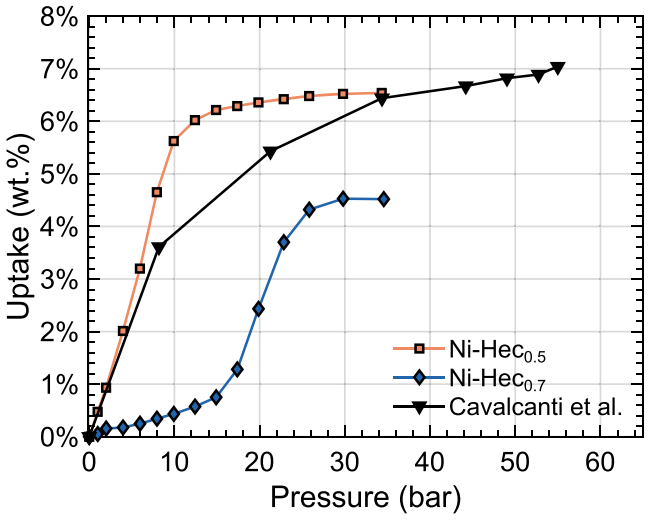

Figure 8. Comparison of the adsorption capacity of Ni-$Hec_{0.5}$ and Ni-$Hec_{0.7}$ compared with results on a Ni-Hec cation-exchanged from a commercial Corning sample.[15]

is difficult as the samples are different in terms of origin, preparation, layer charge, and phase purity. Compared to other clay minerals measured under similar conditions, like dried SWy-2 and STx-1 where a maximum excess adsorption of 0.250−0.650 mmol/g under high pressure has been reported,[4,9−11] our results show a higher adsorption capacity. Compared to the capacity of amine-modified montmorillonite (2.4 mmol/g),[45] our reported capacity is a little lower. However, because both our current and previous[14] investigations indicate that only half of the interlayers are active in the adsorption process, there is a potential to double the capacity if $[Ni(OH)_{2-x}(H_2O)_x]_y^{x+}$ islands can be condensed in all interlayers.

CONCLUSION

Our findings demonstrate that the uptake of CO_2 in the interlayer of a clay mineral increases with a decrease in layer charge. We suggest that this is due to more accessible space and adsorption sites for CO_2 within the interlayers. Moreover, the uptake pressure threshold decreases with a lower layer charge, which we explain by weaker cohesion between the layers.

In future work, these mechanisms will be examined for natural clay minerals, such as montmorillonite. Performing the cation exchange at a slightly increased pH (>8) is shown in the literature[46−48] to produce condensed chlorite-type interlayers only and therefore may double the adsorption capacity for CO_2. Given the compact nature of clay minerals, this can make them volumetrically competitive compared to MOFs and mesoporous carbon.[15] The mechanism for CO_2 capture by clay minerals presented here will also be investigated for a series of transition metals known for their condensation tendency.

The optimum layer charge for Ni-Hec coincides with the layer charge for natural montmorillonite, which is the main ingredient in commercial bentonite. Therefore, the impact of our results could be important for the implementation of clay minerals for industrial carbon capture, separation, and sequestration processes. In addition, as clay minerals are present in cap-rock formations for anthropogenic storage sites, these results provide new knowledge that could be relevant for the long-term stability of such reservoirs.

ASSOCIATED CONTENT

Supporting Information

The Supporting Information is available free of charge at https://pubs.acs.org/doi/10.1021/acs.langmuir.1c02467.

Supporting neutron diffraction, gravimetric adsorption, and X-ray diffraction measurements, sample densities, and a BET isotherm (PDF)

AUTHOR INFORMATION

Corresponding Authors

Kristoffer W. Bø Hunvik − *Department of Physics, Norwegian University of Science and Technology, 7491 Trondheim, Norway;* orcid.org/0000-0002-2684-6464; Email: kristoffer.hunvik@ntnu.no

Jon Otto Fossum − *Department of Physics, Norwegian University of Science and Technology, 7491 Trondheim, Norway;* orcid.org/0000-0002-8952-303X; Email: jon.fossum@ntnu.no

Authors

Patrick Loch − *Bavarian Polymer Institute and Department of Chemistry, University of Bayreuth, D-95447 Bayreuth, Germany*

Dirk Wallacher − *Helmholtz-Zentrum Berlin für Materialien und Energie, 14109 Berlin, Germany*

Alexsandro Kirch − *Departamento de Física dos Materiais e Mecânica, Instituto de Física, Universidade de São Paulo, 05508-090 São Paulo, SP, Brazil*

Leide P. Cavalcanti − *Institute for Energy Technology (IFE), N-2027 Kjeller, Norway;* Present Address: L.P.C.: ISIS Neutron and Muon Source, STFC Rutherford Appleton Laboratory, Chilton OX11 0QX, Didcot, U.K; orcid.org/0000-0002-0408-0058

Martin Rieß − *Bavarian Polymer Institute and Department of Chemistry, University of Bayreuth, D-95447 Bayreuth, Germany*

Matthias Daab − *Bavarian Polymer Institute and Department of Chemistry, University of Bayreuth, D-95447 Bayreuth, Germany*

Vegard Josvanger − *Department of Physics, Norwegian University of Science and Technology, 7491 Trondheim, Norway*

Sven Grätz − *Inorganic Chemistry I, Ruhr-Universität Bochum, 44780 Bochum, Germany*

Fabiano Yokaichiya − *Helmholtz-Zentrum Berlin für Materialien und Energie, 14109 Berlin, Germany*

Kenneth Dahl Knudsen − *Department of Physics, Norwegian University of Science and Technology, 7491 Trondheim, Norway; Institute for Energy Technology (IFE), N-2027 Kjeller, Norway*

Caetano Rodrigues Miranda − *Departamento de Física dos Materiais e Mecânica, Instituto de Física, Universidade de São Paulo, 05508-090 São Paulo, SP, Brazil*

Josef Breu − *Bavarian Polymer Institute and Department of Chemistry, University of Bayreuth, D-95447 Bayreuth, Germany;* orcid.org/0000-0002-2547-3950

Complete contact information is available at: https://pubs.acs.org/10.1021/acs.langmuir.1c02467

Notes

The authors declare no competing financial interest.

■ ACKNOWLEDGMENTS

This work was supported by the Research Council of Norway under the Frinatek Program (Project 250728) and by the Deutsche Forschungsgemeinschaft (SFB 840). P.L. thanks Elite Network Bavaria in the framework of the Elite Study Program "Macromolecular Science" for support. A.K. and C.R.M. gratefully acknowledge the Research Centre for Gas Innovation (RCGI), support from the Brazilian agencies FAPESP (2017/02317-2) and CNPq, and the resources supplied by the Center for Scientific Computing (NCC/GridUNESP) of the São Paulo State University (UNESP). The authors gratefully acknowledge Helmholtz-Zentrum Berlin für Materialien und Energie for granting access to and support for synchrotron and neutron facilities. Measurements were carried out at the KMC-2 instrument beamline at the BESSY II electron storage ring and E2 beamline at the BER II reactor operated by the Helmholtz-Zentrum Berlin für Materialien und Energie. We would like to thank Nico Grimm and Daniel Többens for assistance during the experiment. The research leading to this result has been supported by the project CALIPSOplus under Grant Agreement 730872 from the EU Framework Programme for Research and Innovation HORIZON 2020. Paulo Henrique Michels-Brito and Leander Michels are acknowledged for helpful discussions.

■ REFERENCES

(1) Bowers, G. M.; Loring, J. S.; Schaef, H. T.; Cunniff, S. S.; Walter, E. D.; Burton, S. D.; Larsen IV, R. K.; Miller, Q. R.; Bowden, M. E.; Ilton, E. S.; et al. Chemical trapping of CO2 by clay minerals at reservoir conditions: Two mechanisms observed by in situ high-pressure and-temperature experiments. *ACS Earth and Space Chemistry* **2019**, *3*, 1034−1046.

(2) Bowers, G. M.; Schaef, H. T.; Loring, J. S.; Hoyt, D. W.; Burton, S. D.; Walter, E. D.; Kirkpatrick, R. J. Role of cations in CO2 adsorption, dynamics, and hydration in smectite clays under in situ supercritical CO2 conditions. *J. Phys. Chem. C* **2017**, *121*, 577−592.

(3) Loganathan, N.; Bowers, G. M.; Yazaydin, A. O.; Schaef, H. T.; Loring, J. S.; Kalinichev, A. G.; Kirkpatrick, R. J. Clay swelling in dry supercritical carbon dioxide: effects of interlayer cations on the structure, dynamics, and energetics of CO2 intercalation probed by XRD, NMR, and GCMD simulations. *J. Phys. Chem. C* **2018**, *122*, 4391−4402.

(4) Hwang, J.; Joss, L.; Pini, R. Measuring and modelling supercritical adsorption of CO2 and CH4 on montmorillonite source clay. *Microporous Mesoporous Mater.* **2019**, *273*, 107−121.

(5) Giesting, P.; Guggenheim, S.; Koster van Groos, A. F.; Busch, A. Interaction of carbon dioxide with Na-exchanged montmorillonite at pressures to 640 bars: Implications for CO2 sequestration. *Int. J. Greenhouse Gas Control* **2012**, *8*, 73−81.

(6) Loring, J. S.; Schaef, H. T.; Thompson, C. J.; Turcu, R. V.; Miller, Q. R.; Chen, J.; Hu, J.; Hoyt, D. W.; Martin, P. F.; Ilton, E. S.; Felmy, A. R.; Rosso, K. M. Clay hydration/dehydration in dry to water-saturated supercritical CO2: implications for caprock integrity. *Energy Procedia* **2013**, *37*, 5443−5448.

(7) Loganathan, N.; Yazaydin, A. O.; Kirkpatrick, R. J.; Bowers, G. M. Tuning the Hydrophobicity of Layer-Structure Silicates To Promote Adsorption of Nonaqueous Fluids: Effects of F−for OH− Substitution on CO2 Partitioning into Smectite Interlayers. *J. Phys. Chem. C* **2019**, *123*, 4848−4855.

(8) Schaef, H. T.; Loganathan, N.; Bowers, G. M.; Kirkpatrick, R. J.; Yazaydin, A. O.; Burton, S. D.; Hoyt, D. W.; Thanthiriwatte, K. S.; Dixon, D. A.; McGrail, B. P.; Rosso, K. M.; Ilton, E. S.; Loring, J. S. Tipping point for expansion of layered aluminosilicates in weakly polar solvents: supercritical CO2. *ACS Appl. Mater. Interfaces* **2017**, *9*, 36783−36791.

(9) Rother, G.; Ilton, E. S.; Wallacher, D.; Hauss, T.; Schaef, H. T.; Qafoku, O.; Rosso, K. M.; Felmy, A. R.; Krukowski, E. G.; Stack, A. G.; Grimm, N.; Bodnar, R. J. CO2 sorption to subsingle hydration layer montmorillonite clay studied by excess sorption and neutron diffraction measurements. *Environ. Sci. Technol.* **2013**, *47*, 205−211.

(10) Schaef, H. T.; Davidson, C. L.; Owen, A. T.; Miller, Q. R.; Loring, J. S.; Thompson, C. J.; Bacon, D. H.; Glezakou, V. A.; McGrail, B. P. CO2 utilization and storage in shale gas reservoirs: experimental results and economic impacts. *Energy Procedia* **2014**, *63*, 7844−7851.

(11) Busch, A.; Alles, S.; Gensterblum, Y.; Prinz, D.; Dewhurst, D. N.; Raven, M. D.; Stanjek, H.; Krooss, B. M. Carbon dioxide storage potential of shales. *Int. J. Greenhouse Gas Control* **2008**, *2*, 297−308.

(12) Hemmen, H.; Rolseth, E. G.; Fonseca, D. M.; Hansen, E. L.; Fossum, J. O.; Plivelic, T. S. X-ray studies of carbon dioxide intercalation in Na-fluorohectorite clay at near-ambient conditions. *Langmuir* **2012**, *28*, 1678−1682.

(13) Michels, L.; Fossum, J. O.; Rozynek, Z.; Hemmen, H.; Rustenberg, K.; Sobas, P. A.; Kalantzopoulos, G. N.; Knudsen, K. D.; Janek, M.; Plivelic, T. S.; da Silva, G. J. Intercalation and retention of carbon dioxide in a smectite clay promoted by interlayer cations. *Sci. Rep.* **2015**, *5*, 8775.

(14) Hunvik, K. W. B.; Loch, P.; Cavalcanti, L. P.; Seljelid, K. K.; Røren, P. M.; Rudić, S.; Wallacher, D.; Kirch, A.; Knudsen, K. D.; Rodrigues Miranda, C.; Breu, J.; Bordallo, H. N.; Fossum, J. O. CO2 Capture by Nickel Hydroxide Interstratified in the Nanolayered Space of a Synthetic Clay Mineral. *J. Phys. Chem. C* **2020**, *124*, 26222−26231.

(15) Cavalcanti, L. P.; Kalantzopoulos, G. N.; Eckert, J.; Knudsen, K. D.; Fossum, J. O. A nano-silicate material with exceptional capacity for CO 2 capture and storage at room temperature. *Sci. Rep.* **2018**, *8*, 11827.

(16) Busch, A.; Bertier, P.; Gensterblum, Y.; Rother, G.; Spiers, C.; Zhang, M.; Wentinck, H. M. On sorption and swelling of CO 2 in clays. *Geomechanics and Geophysics for Geo-energy and Geo-resources* **2016**, *2*, 111−130.

(17) Bergaya, F.; Lagaly, G. *Handbook of clay science*; Newnes, 2013.

(18) Michot, L. J.; Bihannic, I.; Pelletier, M.; Rinnert, E.; Robert, J.-L. Hydration and swelling of synthetic Na-saponites: Influence of layer charge. *Am. Mineral.* **2005**, *90*, 166−172.

(19) Vinci, D.; Dazas, B.; Ferrage, E.; Lanson, M.; Magnin, V.; Findling, N.; Lanson, B. Influence of layer charge on hydration properties of synthetic octahedrally-charged Na-saturated trioctahedral swelling phyllosilicates. *Appl. Clay Sci.* **2020**, *184*, 105404.

(20) Ferrage, E.; Lanson, B.; Michot, L. J.; Robert, J.-L. Hydration properties and interlayer organization of water and ions in synthetic Na-smectite with tetrahedral layer charge. Part 1. Results from X-ray diffraction profile modeling. *J. Phys. Chem. C* **2010**, *114*, 4515−4526.

(21) Ferrage, E.; Sakharov, B. A.; Michot, L. J.; Delville, A.; Bauer, A.; Lanson, B.; Grangeon, S.; Frapper, G.; Jiménez-Ruiz, M.; Cuello, G. J. Hydration properties and interlayer organization of water and ions in synthetic Na-smectite with tetrahedral layer charge. Part 2. Toward a precise coupling between molecular simulations and diffraction data. *J. Phys. Chem. C* **2011**, *115*, 1867−1881.

(22) Jiménez-Ruiz, M.; Ferrage, E.; Delville, A.; Michot, L. Anisotropy on the collective dynamics of water confined in swelling clay minerals. *J. Phys. Chem. A* **2012**, *116*, 2379−2387.

(23) Dazas, B.; Lanson, B.; Delville, A.; Robert, J.-L.; Komarneni, S.; Michot, L. J.; Ferrage, E. Influence of tetrahedral layer charge on the organization of interlayer water and ions in synthetic Na-saturated smectites. *J. Phys. Chem. C* **2015**, *119*, 4158−4172.

(24) Gates, W. P.; Bordallo, H. N.; Aldridge, L. P.; Seydel, T.; Jacobsen, H.; Marry, V.; Churchman, G. J. Neutron time-of-flight quantification of water desorption isotherms of montmorillonite. *J. Phys. Chem. C* **2012**, *116*, 5558−5570.

(25) Michot, L. J.; Ferrage, E.; Delville; Jiménez-Ruiz, M. Influence of layer charge, hydration state and cation nature on the collective

https://doi.org/10.1021/acs.langmuir.1c02467
Langmuir 2021, 37, 14491−14499

dynamics of interlayer water in synthetic swelling clay minerals. *Appl. Clay Sci.* **2016**, *119*, 375−384.
(26) Rao, Q.; Leng, Y. Effect of layer charge on CO2 and H2O intercalations in swelling clays. *Langmuir* **2016**, *32*, 11366−11374.
(27) Bowers, G. M.; Loring, J. S.; Walter, E. D.; Burton, S. D.; Bowden, M. E.; Hoyt, D. W.; Arey, B.; Larsen IV, R. K.; Kirkpatrick, R. J. Influence of Smectite Structure and Hydration on Supercritical Methane Binding and Dynamics in Smectite Pores. *J. Phys. Chem. C* **2019**, *123*, 29231−29244.
(28) Rosenfeldt, S.; Stöter, M.; Schlenk, M.; Martin, T.; Albuquerque, R. Q.; Förster, S.; Breu, J. In-depth insights into the key steps of delamination of charged 2D nanomaterials. *Langmuir* **2016**, *32*, 10582−10588.
(29) Stöter, M.; Kunz, D. A.; Schmidt, M.; Hirsemann, D.; Kalo, H.; Putz, B.; Senker, J.; Breu, J. Nanoplatelets of sodium hectorite showing aspect ratios of 20 000 and superior purity. *Langmuir* **2013**, *29*, 1280−1285.
(30) Loch, P.; Hunvik, K. W. B.; Puchtler, F.; Weiß, S.; Seljelid, K. K.; Røren, P. M.; Rudic, S.; Raaen, S.; Knudsen, K. D.; Bordallo, H. N.; Fossum, J. O.; Breu, J. Spontaneous formation of an ordered interstratification upon Ni-exchange of Na-fluorohectorite. *Appl. Clay Sci.* **2020**, *198*, 105831.
(31) Altoé, M. A. S.; Michels, L.; dos Santos, E. C.; Droppa, R., Jr; Grassi, G.; Ribeiro, L.; Knudsen, K.; Bordallo, H. N.; Fossum, J. O.; da Silva, G. J. Continuous water adsorption states promoted by Ni2+ confined in a synthetic smectite. *Appl. Clay Sci.* **2016**, *123*, 83−91.
(32) Daab, M.; Eichstaedt, N. J.; Habel, C.; Rosenfeldt, S.; Kalo, H.; Schießling, H.; Förster, S.; Breu, J. Onset of Osmotic Swelling in Highly Charged Clay Minerals. *Langmuir* **2018**, *34*, 8215−8222.
(33) Daab, M.; Eichstaedt, N. J.; Edenharter, A.; Rosenfeldt, S.; Breu, J. Layer charge robust delamination of organo-clays. *RSC Adv.* **2018**, *8*, 28797−28803.
(34) Mermut, A. R.; Lagaly, G. Baseline studies of the clay minerals society source clays: layer-charge determination and characteristics of those minerals containing 2:1 layers. *Clays Clay Miner.* **2001**, *49*, 393−397.
(35) Többens, D. M.; Zander, S. KMC-2: an X-ray beamline with dedicated diffraction and XAS endstations at BESSY II. *Journal of Large-Scale Research Facilities* **2016**, *2*, 49.
(36) Lemmon, E. W.; McLinden, M. O.; Friend, D. G. Thermophysical Properties of Fluid Systems. NIST Standard Reference Database Number 69 (accessed 2020-06-22).
(37) Soler, J. M.; Artacho, E.; Gale, J. D.; García, A.; Junquera, J.; Ordejón, P.; Sánchez-Portal, D. The SIESTA method for ab initio order-N materials simulation. *J. Phys.: Condens. Matter* **2002**, *14*, 2745.
(38) Berland, K.; Hyldgaard, P. Exchange functional that tests the robustness of the plasmon description of the van der Waals density functional. *Phys. Rev. B: Condens. Matter Mater. Phys.* **2014**, *89*, 035412.
(39) Herling, M. M.; Kalo, H.; Seibt, S.; Schobert, R.; Breu, J. Tailoring the pore sizes of microporous pillared interlayered clays through layer charge reduction. *Langmuir* **2012**, *28*, 14713−14719.
(40) Lagaly, G. Layer charge heterogeneity in vermiculites. *Clays Clay Miner.* **1982**, *30*, 215−222.
(41) Malikova, N.; Cadene, A.; Dubois, E.; Marry, V.; Durand-Vidal, S.; Turq, P.; Breu, J.; Longeville, S.; Zanotti, J.-M. Water diffusion in a synthetic hectorite clay studied by quasi-elastic neutron scattering. *J. Phys. Chem. C* **2007**, *111*, 17603−17611.
(42) Weiss, A.; Becker, H.; Orth, H.; Mai, G.; Lechner, H.; Range, K. Particle size effects and reaction mechanism of the intercalation into kaolinite. *Proceedings of the International Clay Conference, Tokyo*; 1969; pp 180−184.
(43) Stöcker, M.; Seyfarth, L.; Hirsemann, D.; Senker, J.; Breu, J. Microporous PILCs—Synthesis, pillaring mechanism and selective cation exchange. *Appl. Clay Sci.* **2010**, *48*, 146−153.
(44) Laird, D. A. Influence of layer charge on swelling of smectites. *Appl. Clay Sci.* **2006**, *34*, 74−87.
(45) Stevens, L.; Williams, K.; Han, W. Y.; Drage, T.; Snape, C.; Wood, J.; Wang, J. Preparation and CO2 adsorption of diamine modified montmorillonite via exfoliation grafting route. *Chem. Eng. J.* **2013**, *215*, 699−708.
(46) Ohtsuka, K.; Suda, M.; Tsunoda, M.; Ono, M. Synthesis of metal hydroxide-layer silicate intercalation compounds (metal= Mg (II), Ca (II), Mn (II), Fe (II), Co (II), Ni (II), Zn (II), and Cd (II)). *Chem. Mater.* **1990**, *2*, 511−517.
(47) Uehara, M.; Yamzaki, A.; Umezawa, T.; Takahashi, K.; Tsutsumi, S. A nickel hydroxide-vermiculite complex: Preparation and characterization. *Clays Clay Miner.* **1999**, *47*, 726−731.
(48) Yamanaka, S.; Brindley, G. Hydroxy-nickel interlayering in montmorillonite by titration method. *Clays Clay Miner.* **1978**, *26*, 21−24.

https://doi.org/10.1021/acs.langmuir.1c02467
Langmuir 2021, 37, 14491−14499